

Virial Equation of State of Helium, Xenon, and Helium–Xenon Mixtures from Speed-of-Sound and Burnett $P\rho T$ Measurements

J. J. Hurly,¹ J. W. Schmidt,¹ S. J. Boyes,^{1,2} and M. R. Moldover^{1,3}

Received May 29, 1996

The virial equation of state was determined for helium, xenon, and helium–xenon mixtures for the pressure and temperature ranges 0.5 to 5 MPa and 210 to 400 K. Two independent experimental techniques were employed: Burnett $P\rho T$ measurements and speed-of-sound measurements. The temperature-dependent second and third density virial coefficients for pure xenon and the second and third interaction density virial coefficients for helium–xenon mixtures were determined. The present density virial equations of state for xenon and helium–xenon mixtures reproduce the speed-of-sound data within 0.01% and the $P\rho T$ data within 0.02% of the pressures. All the results for helium are consistent, within experimental errors, with recent ab initio calculations, confirming the accuracy of the experimental techniques.

KEY WORDS: equation-of-state; helium; helium-xenon mixture; speed-of-sound; thermoacoustic refrigerators; thermodynamic properties; virial coefficients; xenon.

1. INTRODUCTION

Helium–xenon mixtures are the optimum working fluid in thermoacoustic refrigerators because they have very low Prandtl numbers. This potential application has led us to acquire the data needed to refine the equation of state for these mixtures under conditions that include those most widely encountered in experimental thermoacoustic refrigerators. The present

¹ Thermophysics Division, Chemical Science and Technology Laboratory, National Institute of Standards and Technology, Gaithersburg, Maryland 20899, U.S.A.

² Present address: Centre for Quantum Metrology, National Physical Laboratory, Teddington, Middlesex TW11 0LW, United Kingdom.

³ To whom correspondence should be addressed.

results were obtained with two laboratory systems for determining accurate gas compressibility factors and the associated virial coefficients. One is a Burnett apparatus for measuring the equation of state at pressures up to 20 MPa over a temperature range of 273 to 473 K; the other is an automated speed-of-sound system operating at pressures up to 1.5 MPa over the temperature range 210 to 400 K. Both apparatuses were employed in this study of helium, xenon, and three helium-xenon mixtures.

For helium, the present Burnett density-pressure-temperature data $\rho(P, T)$ span the temperature range 273 to 373 K with pressures to 5 MPa. The present speed-of-sound data $u(P, T)$ for helium span the temperature range of 225 to 300 K with pressures up to 1.5 MPa. Both the $\rho(P, T)$ data and the $u(P, T)$ data were compared with *ab initio* calculations of these properties. To make this comparison, only one apparatus parameter was fitted to the data, namely, the "cell constant," which is the ratio of the two Burnett volumes. Nearly all the $\rho(P, T)$ data agreed with the *ab initio* values within $\pm 0.01\%$ of P (or ρ) and nearly all the $u(P, T)$ data agreed with the *ab initio* values within $\pm 0.01\%$ of u . The agreement demonstrates the high accuracy and precision of these experimental techniques.

Xenon was also studied with both the Burnett and the speed-of-sound systems. The $\rho(P, T)$ data fall in the range $263 \leq T \leq 358$ K and $P < 3$ MPa. The $u(P, T)$ data fall in the range $210 \leq T \leq 400$ K and $P < 1.4$ MPa or 80% of the vapor pressure, whichever is less. Both sets of data were simultaneously fitted by the density virial equation of state

$$P = RT\rho[1 + B(T)\rho + C(T)\rho^2 + D(T)\rho^3 + \dots] \quad (1)$$

truncated after the second and third density virial coefficients $B(T)$ and $C(T)$. The temperature dependencies of $B(T)$ and $C(T)$ were assumed to be those of hard-core square-well interatomic potentials. With this assumption, fitting Eq. (1) to the $\rho(P, T)$ data is straightforward. Fitting the $u(P, T)$ data was facilitated by using analytic expressions for the density virial coefficients and the exact thermodynamic relationships (summarized below) connecting $u(P, T)$ to the density virial equation of state. In the range of the present data, the fitted values of $B(T)$ agree with previously published values to within combined uncertainties and they also agree with the values calculated from a realistic interatomic potential function. The present measurements greatly reduce the uncertainty of $B(T)$ of xenon. We also report values for $C(T)$ of xenon. Previously reported values spanned the range 273 to 400 K. Here we successfully extended the temperature range down to 210 K, while simultaneously reducing the uncertainty in $C(T)$. The virial equation of state presented here reproduces nearly all the $\rho(P, T)$ data to within $\pm 0.02\%$ of P (or ρ) and nearly all the $u(P, T)$ data

to within $\pm 0.01\%$ of u . The $\rho(P, T)$ data in the range $2 \leq P \leq 3$ MPa were not used in the fit and show systematic deviations from the best fit; thus, these data contain information about $D(T)$ for xenon that we have not exploited.

Finally, three helium–xenon mixtures with the nominal compositions of 74/26, 47/53, and 20/80 mol% helium to xenon were studied in the temperature range of 210 to 400 K and at pressures up to 5 MPa. All of the experimental results for the three mixtures together with the *ab initio* results for helium, and our accurate second and third density virial coefficients for xenon, were simultaneously fit to a density virial equation-of-state surface for helium–xenon mixtures. In this fit, $B(T)$ and $C(T)$ for helium and xenon had been determined already from the data for the pure gases; thus, the interaction second and third density virial coefficients, $B_{12}(T)$, $C_{112}(T)$, and $C_{122}(T)$ were the only parameters used to fit all of the mixture data. Their temperature dependencies were represented by polynomial functions of $1/T$. With these parameters, the virial equation of state reproduces nearly all the speed-of-sound data to within $\pm 0.01\%$ of u and nearly all the Burnett data to within $\pm 0.02\%$ of the pressure (or density). Within the experimental uncertainties, the present data agree with the more limited, previously published mixture data. Our values for $B_{12}(T)$ are within $1 \text{ cm}^3 \cdot \text{mol}^{-1}$ of those calculated from realistic intermolecular potentials determined from multiproperty fits; our values are as much as $3 \text{ cm}^3 \cdot \text{mol}^{-1}$ above those from a law-of-corresponding-states model.

2. EXPERIMENTAL TECHNIQUES

2.1. Burnett Measurements

A detailed description of the Burnett apparatus has been given elsewhere [1–3]. Briefly, the apparatus consisted of two cylindrical vessels with volumes $V_1 \approx 27 \text{ cm}^3$ and $V_2 \approx 18 \text{ cm}^3$. These volumes had been bored out from opposite ends of a single nickel cylinder. The first volume, V_1 , was the sample volume and it was bound at one end by a highly sensitive home-made capacitance diaphragm transducer [4]. The transducer was an integral part of V_1 and it was used as a null detector when balancing the pressure of the sample gas in V_1 with the pressure of the argon in a manifold that led from V_1 to the pressure gauges and the pressure controller. The pressure of the argon was measured with either a quartz bourdon-tube gauge or a pneumatic deadweight piston gauge in conjunction with a calibrated barometer. The sample volume and expansion volumes, including piping and transducer spaces, were in a thermostated bath that

was stable within approximately 1 mK at each set point. The gradients within the bath were several millikelvins. The temperature was measured with a standard platinum resistance thermometer connected to a high-precision multimeter.

For measuring the equation of state of xenon, the Burnett apparatus was used in the traditional Burnett mode. The measurements on each isotherm began by filling the sample volume V_1 to a high initial pressure and then allowing temperature and pressure to equilibrate. The argon pressure was adjusted until the capacitance diaphragm transducer was balanced; then the argon pressure was measured and recorded as P_0 . The corresponding compressibility factor was $Z_0 = P_0 V_1 (P_0, T) / n_0 RT$. [The notation $V_1(P_0, T)$ indicates that the pressure and temperature dependencies of V_1 were accounted for. Here, R denotes the universal gas constant and n_0 is the number of moles in the initial sample.] The gas was then allowed to expand into the expansion volume, V_2 . The temperature and pressure were again allowed to equilibrate and the new compressibility factor following the first expansion was $Z_1 = P_1 [V_1(P_1, T) + V_2(P_1, T)] / n_0 RT$. The sample volume was isolated and V_2 was evacuated. The expansion was repeated and the equilibrium pressure was measured again. This process was repeated until the pressure was of the order of 200 kPa.

Further expansions would not have been useful because of the limited resolution of the pressure measurement. The ratio of the i th expansion to the $(i-1)$ th expansion yields $P_{i-1}/P_i = N(P_i, P_{i-1}, T)Z_{i-1}/Z_i$. Combining this relation with $P = \rho ZRT$ leads to $\rho_i = \rho_{i-1}/N$. The cell constant $N \equiv (V_1 + V_2)/V_1$ is the ratio of the volume following the i th expansion to the volume preceding the expansion. From the present helium data it was determined to be $N = 1.781327 \pm 0.000035$, where the uncertainty quoted is one standard deviation. (In principle, the cell constant is a weak function of the pressure; however, this was neglected.) An isotherm results in a series of equations which can be solved approximately with a nonlinear regression resulting in reduced data in the form $\rho(P)$ for each isotherm. The data for all the isotherms were then fitted by the virial equation of state to obtain the temperature-dependent density virial coefficients.

The Burnett apparatus, operated as described above, yields data of the highest accuracy consistent with the capability of the apparatus. Unfortunately, this mode of operation was very labor intensive. The measurements on each isotherm required frequent manual operation of delicate valves with a torque wrench and frequent manual pressure measurements with a piston gauge referenced to a calibrated barometer. In this mode, the standard deviation of the pressure measurements was

$$\sigma_p = \sqrt{(44 \times 10^{-6} P)^2 + (10 \text{ Pa})^2} \quad (2)$$

The alternative mode of operating the Burnett apparatus was to make automated pressure and temperature measurements on isochores and to determine the densities of the isochores by Burnett expansions on a single isotherm. This alternative was used for pure helium and for the three helium–xenon mixtures. In this mode, after V_1 was filled and valved off at the highest pressure P_0 on the highest isotherm T_0 , the temperature was reduced in steps under computer control while the pressure was monitored with the quartz bourdon tube gauge. Thus, the equation of state was measured on a quasi-isochoke without operator intervention. (If the thermal and pressure expansion of V_1 could have been ignored, then the data would have been exactly on an isochore.) The apparatus was returned to T_0 and a single Burnett expansion was made to the pressure P_1 . Then, the equation of state was measured on the second quasi-isochoke starting at the state (P_1, T_0) and the apparatus was returned to T_0 . This process was repeated until the Burnett expansions on T_0 brought the pressure to 200 kPa. In this way, the entire equation of state was measured with only slightly more effort than that required for a single isotherm. However, the accuracy was reduced for several reasons. One is that the quartz bourdon tube gauge was neither as accurate nor as stable as the piston gauge. When the pressure was measured manually with the bourdon tube gauge, its standard deviation was

$$\sigma_p = \sqrt{(50 \times 10^{-6} P)^2 + (37 \text{ Pa})^2} \quad (3)$$

In automatic operation, the dead band of the pressure servosystem contributed an additional ± 80 Pa to the uncertainties of the pressure measurement. In that case,

$$\sigma_p = \sqrt{(50 \times 10^{-6} P)^2 + (88 \text{ Pa})^2} \quad (4)$$

In automatic operation, very slow drifts in the thermometry may have reduced the precision of the Burnett data on T_0 because it took more than one week to complete the isotherm. (The uncertainty of the data was dominated by the uncertainty of the pressure measurement.) Finally, in automated operation, the thermal expansion of the volume V_1 must be accounted for. The densities on the helium isochores were related to the volumetric thermal expansion coefficient $\beta(T)$ via

$$\rho = (\rho_0 / N^i) \left[1 - \int_{T_0}^T \beta(T) dT \right] \quad (5)$$

Here, $T_0 \equiv 273.15$ K and ρ_0 is the initial density of the sample on the Burnett isotherm and is sometimes called the “run constant.” We used the

function $\beta(T) = [37 + 0.038(T - 273)] \times 10^{-6}$, where T is in K, to represent the volumetric expansion; it was obtained from published [5] data for the linear thermal expansion.

2.2. Speed-of-Sound Measurements

Our laboratory has developed an automated apparatus [6-11] to measure the speed of sound in gases with a high accuracy. This apparatus has been used to study more than 20 gases and gas mixtures [12-19]. A detailed description of the apparatus and the elaborate acoustic model used to reduce the data has been given in previous publications [17, 18].

The heart of the apparatus was an acoustic resonator. The resonator was a heavy-walled, 14-cm-long, cylindrical cavity that had been bored out of a stainless-steel cylinder. The cavity had an inner diameter of 6.5 cm and an outer diameter 7.8 cm. Circular stainless-steel plates (1.3 cm thick) were sealed to the end of the cavity with gold O-rings. One end plate contained two thin metal diaphragms mounted flush with the interior surface of the cavity [11]. These diaphragms isolated the sample gas while coupling acoustic energy into and out of the cavity. The diaphragms were stainless-steel disks (1 cm in diameter, 25 μm thick) that had been electron beam welded around their circumferences to small flanges.

Acoustic wave guides connected the diaphragms to two remote electroacoustic transducers at ambient temperature. When sample gas was present in the resonator cavity, a pressure controller maintained an equal pressure of argon in the wave guides. Thus, the metal diaphragms were not stretched by a differential pressure. The wave guides were commercially purchased horn-shaped tubes with a length of 15 cm and a diameter that tapered exponentially from 0.12 to 0.33 cm. A 2.5-cm-long, thin-walled, stainless-steel tube connected the horns to gas-tight transducer housings that were also maintained at the same pressure as the sample gas. A metal screen located at the narrow end of the horn damped spurious resonances within the wave guides. When the wave guides were filled with argon, they strongly attenuated sound at frequencies above 8 kHz.

The source transducer was a commercially manufactured earphone capable of dissipating a few watts. It acted as a loud speaker emitting sound that was transmitted down a wave guide through one metal diaphragm into the resonator. The acoustic energy within the resonator was coupled through the second metal diaphragm up the second wave guide to the sound detector, which was a commercially manufactured hearing aid.

The frequency of the source was scanned through several resonances. The frequency f and the width g of each resonance were measured using

standard procedures [9] and instruments, typically with an uncertainty of less than 1×10^{-5} of the frequency. Except for the measurements with pure helium, three modes were used, namely, (3, 0, 0), (4, 0, 0), and (0, 0, 1). (The modes are labeled with the notation of Gillis [17].) The speed of sound and its uncertainty were computed from weighted averages of the results for the three modes. The fractional inconsistencies among the modes ranged from (1 to 20) $\times 10^{-5}$, varying roughly as P^{-2} .

The resonator was suspended vertically in a well-stirred thermostatted bath of either silicon oil or methanol. The bath was controlled within 1 mK of the set-point. A 25- Ω capsule-type standard platinum resistance thermometer (SPRT) was mounted in an aluminum block in thermal equilibrium with the resonator. Four-wire resistance measurements of the SPRT were performed by a high-precision dc multimeter. All temperatures are reported on ITS-90.

A 13-kPa full-scale capacitance differential pressure transducer (DPT) was used to detect the balance of pressure between the argon and the sample gas. The DPT was calibrated for pressure and temperature dependence and it was thermostated near 333 K with a stability of ± 0.1 K. Pressure measurements were made on the argon side of the DPT with a quartz boundon tube differential pressure gauge. The reference side of the gauge was maintained below 2 Pa with a rotary pump. This bourdon tube gauge had been calibrated with a deadweight gauge to a standard uncertainty of $\sigma_p = 30 \text{ Pa} + 0.0001 \times P$.

Measurements on each isotherm were performed by first loading the resonator to either 1.5 MPa or 80% of the sample's vapor pressure, whichever was less. The temperature and pressure were allowed to equilibrate, and the frequencies and widths of the acoustic resonances were measured. The temperature was maintained, and the pressure dropped in successive steps. Again, the apparatus was allowed to return to equilibrium and the frequencies and widths were measured.

The effective radius and length of the cylindrical resonator were accurately determined as functions of the temperature by measuring the resonance frequencies when the resonator was filled with argon, a gas for which the speed of sound is accurately known. Because the calibration and the present measurements were conducted in the same bath, there is a high degree of compensation for the effects of temperature gradients in the bath and for errors in the measurement of temperature.

3. EXPERIMENTAL PROBLEMS

Prior to this work, the speed-of-sound measurement system had been used to study more than 20 other gases and gas mixtures at the temperatures

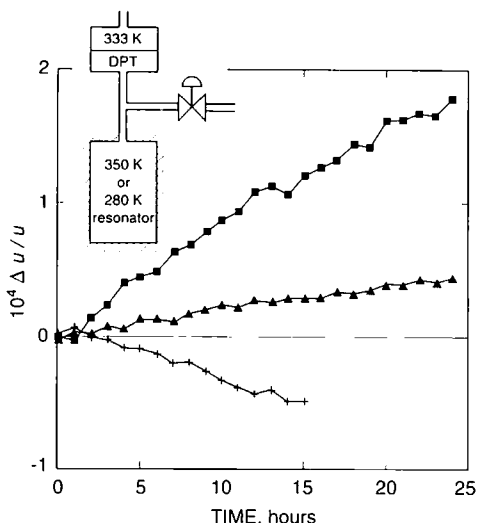


Fig. 1. Time dependence of the speed of sound in the 74/26 helium/xenon mixture at constant pressure and temperature. (■) 350 K at 200 kPa; (▲) 350 K at 1000 kPa; (+) 280 K at 200 kPa.

and pressures encountered in this work. Despite this extensive experience, unanticipated experimental problems occurred. One set of problems resulted from the fact that the speed of sound in helium is much higher than the speed of sound in the other gases that had been studied. A second set of problems resulted from fractionation of the helium–xenon mixtures via thermal diffusion within the tube that led from the resonator in the thermostated bath to the DPT that was thermostated at 333 K (see Fig. 1). Thermal diffusion is more rapid in helium–xenon mixtures than in the other mixtures that we had studied and its effects are more noticeable because the speed of sound is so much greater in helium than in xenon. First, we describe the problems with the helium measurements and then the problems with the mixtures.

3.1. Helium

When the present resonator was filled with helium, the lowest radial acoustic mode had resonances that ranged from 16 to 22 Hz as the temperature was varied. The argon-filled wave guides have a cutoff frequency near 8 kHz, making these frequencies undetectable. The wave guides could not be filled with helium at high pressures because the helium would have come in contact with the quartz bourdon tube gauge and altered its

calibration in an unpredictable fashion. Only the first (1, 0, 0) and second (2, 0, 0) longitudinal resonance frequencies could be measured. The modes are identified with the notation of Ref. 17. Second, near 330 K, the frequency of the (2, 0, 0) frequency coincided with a resonance in the structure comprising the resonator near $f = 7.6$ kHz. Thus, even the (2, 0, 0) mode was not useful for accurate measurements at the higher pressures where the acoustic resonances in the gas interact most strongly with the structural resonances. Finally, the data for the (1, 0, 0) mode at 400 and 350 K were also found to approach a shell resonance near $f = 3.8$ kHz and were not used in the analysis; however, they are tabulated. In the worst case, which occurred at the highest temperature and pressure, these data differed from the *ab initio* results by 0.035 % of the speed of sound.

The experimental signature [9, 10] of the interaction of a structural resonance with an acoustic resonance of the gas within the resonator is an anomalous increase in the width g of the acoustic resonance and an anomalous shift in its frequency f that is proportional to the pressure. Thus, we were able to verify the presence of the structural resonances by filling the resonator with argon at 1.4 MPa and measuring the frequencies of the first seven longitudinal resonances of the gas while the speed or sound was changed by sweeping the temperature. The structural resonances were manifest by anomalies in the temperature dependencies of the frequencies and of the widths of the (3, 0, 0) and (6, 0, 0) modes of the argon-filled resonator. These anomalies occurred at the same frequencies as the anomalies that were detected in the (1, 0, 0) and (2, 0, 0) modes of the helium-filled resonator.

Among all 20+ gases that we have studied with this apparatus, helium has the highest mean free path at any specified pressure. Thus, it has the highest thermal conductivity κ and it also has the large value 2/3 for the specific heat ratio $(C_p - C_v)/C_v$. Because $g/f \propto \kappa^{1/2}(C_p - C_v)/C_v$, the widths of acoustic resonances in helium were much broader than in the other gases. It follows that the signal-to-noise ratios of the acoustic measurements in helium were much lower than in other gases. This was a nuisance rather than a problem because neither the accuracy nor the precision of the present measurements was limited by noise.

3.2. Helium–Xenon Mixture Composition Shifts

The apparent speed of sound in the helium–xenon mixtures exhibited an easily detected time dependence that is documented in Fig. 1 for the 74/26 helium/xenon mixture. The time dependence varied inversely as the pressure of the sample and directly as the difference between the temperature of the resonator and the temperature of the differential pressure

transducer (DPT) that separated the sample from the pressure balancing system. We attributed the changes in the speed of sound to fractionation of the sample via thermal diffusion in the tube that passed through the temperature gradient that existed between the resonator and the DPT (see Fig. 1). As fractionation progressed, the average molecular weight of the portion of the sample within the resonator changed and the speed of sound in that portion, which varies inversely as the square root of the molecular weight, also changed.

The inset in Fig. 1 is a sketch indicating the location of the thermal gradients on the relevant portions of the speed-of-sound apparatus. For the data displayed in Fig. 1, the resonator was maintained in a well-stirred bath at either 280 or 350 K. A 3.2-mm ($\frac{1}{8}$ -in.)-O.D. tube led from the bottom of the resonator out the top of the bath to a tee in the ambient air. Similar tubes led from the tee to an air-operated valve at ambient temperature and to the DPT that was maintained at 333 K. The valve was usually closed; it was opened only when the pressure of the sample was changed.

The temperature gradient sets up a gradient of chemical potential between the larger resonator volume and the smaller volume of the DPT. In helium/xenon mixtures, the helium concentration will decrease in the colder volume until the chemical potential gradient vanishes. This model explains the shifts observed in the speed of sound. When the resonator was above 333 K, the helium concentration in the colder DPT decreased and the speed of sound of the gas remaining in the resonator increased as the average molecular weight of the sample in the resonator decreased. When the resonator was below 333 K the speed of sound decreased as the helium concentration in the resonator decreased.

For the 74/26 helium/xenon mixture at 0.2 MPa at 350 K, the increase in the speed of sound during 24 h was equivalent to a 20×10^{-6} increase in the mole fraction of helium. At 1.0 MPa and 350 K, the increase was equivalent to a 4×10^{-6} increase in the mole fraction of helium. These results are consistent with the inverse pressure dependence of diffusion. The derivative of the speed of sound with respect to mole fraction du/dx is

$$(2/u)(du/dx) = -[1 - (m_{\text{He}}/m_{\text{Xe}})]/[1 - x - (m_{\text{He}}/m_{\text{Xe}})]$$

where $m_{\text{He}}/m_{\text{Xe}} \approx 0.03$ is the ratio of the molecular mass of helium to that of xenon. The derivative is twice as large in the 74/26 mixture as in the 47/53 mixture and it is three times as large in the 74/26 mixture as in the 20/80 mixture. Thus, the effect of fractionation was most evident for the 74/25 mixture.

Once we understood the origin of the fractionation that occurred, we discarded the speed-of-sound measurements below 0.4 MPa. Typically, it

took 4 h to measure the speed of sound from 1.5 to 0.4 MPa on an isotherm. The normal experimental uncertainties would be larger than the fractionation that occurred during the comparatively short residence of the sample at these comparatively high pressures. We verified this by filling the resonator with a fresh aliquot of the 74/26 mixture at 0.4 MPa and promptly measuring the speed of sound. Within experimental error, the prompt measurement agreed with the results obtained by the usual protocol of filling the resonator at 1.5 MPa and measuring the speed of sound as the pressure was reduced in successive steps.

4. ANALYSIS AND RESULTS

Our analysis is based on the density virial equation of state. As mentioned above and detailed below, we used simple algebraic expressions to represent the temperature dependencies of $B(T)$ and $C(T)$. To fit the $\rho(P, T)$ data and the $u(P, T)$ data simultaneously, we required expressions for $u(P, T)$ in terms of the virial coefficients. Here we list there expressions for the case where $D(T)$ and the higher density virial coefficients are exactly zero [20].

$$u^2 = \frac{\gamma^0 RT}{m} \left(1 + \frac{\beta_a P}{RT} + \frac{\gamma_a p^2}{RT} + \frac{\delta_a p^3}{RT} + \dots \right) \quad (6)$$

where the acoustic virial coefficients β_a , γ_a , and δ_a are related to B , C , and γ^0 by

$$\beta_a = 2B + 2(\gamma^0 - 1) B_t + \frac{(\gamma^0 - 1)^2}{\gamma^0} B_u \quad (7)$$

$$\gamma_a = (L - \beta_a B)/(RT)$$

$$\delta_a = (M - \beta_a C - 2RT\gamma_a B)/(RT)^2$$

$$\gamma^0 L = (\gamma^0 - 1) Q^2 + (2\gamma^0 + 1) C + (\gamma^{02} - 1) C_t + \frac{(\gamma^0 - 1)^2}{2} C_u \quad (8)$$

$$\gamma^0 M = (\gamma^0 - 1)^2 Q^2 (2B_t + B_u) + (\gamma^0 - 1) QP \quad (9)$$

where

$$P = 2C + 2\gamma^0 C_t + (\gamma^0 - 1) C_u$$

and

$$Q = B + (2\gamma^0 - 1) B_t + (\gamma^0 - 1) B_u$$

Here we have introduced the notation $A_t \equiv T(dA/dT)$ and $A_u \equiv T^2(d^2A/dT^2)$ and, as is customary, $\gamma^0 \equiv C_p^0/C_v^0$ is the zero-pressure limit of the heat-capacity ratio. For the monatomic gases $\gamma^0 = 5/3$.

Note that δ_a and the higher-order acoustic virial coefficients depend on the derivatives of $B(T)$ and $C(T)$; thus, they must be accounted for in the calculation of $u(P, T)$, even when the density expansion, Eq. (1), is limited to two terms [20]. For the present data, we verified that ε_a could be neglected.

A nonlinear fitting algorithm [21] was employed to determine the parameters defining $B(T)$ and $C(T)$ by simultaneously fitting the $\rho(P, T)$ and $u(P, T)$ data to Eq. (1). For both sets of data, the uncertainty in the temperature was negligible. The $\rho(P, T)$ data were weighted inversely as the square of the estimated standard deviation of the pressure. Equation (2) for σ_p was used for all the xenon $\rho(P, T)$ data and for the helium and mixture data near 373 K; Eq. (4) was used for the rest of the $\rho(P, T)$ data. The $u(P, T)$ data were weighted inversely as σ_u^2 , the square of the estimated standard deviation of the speed of sound. For states where several resonance frequencies could be measured, σ_u^2 was calculated from a weighted average of the frequencies of the various modes. For xenon, $1 \times 10^{-5} < \sigma_u/u < 20 \times 10^{-5}$; the average value of σ_u/u was 5×10^{-5} and it varied very approximately as P^{-2} . For the mixtures, $1 \times 10^{-5} < \sigma_u/u < 15 \times 10^{-5}$ and the average value of σ_u/u was 6×10^{-5} . For helium, only one frequency was available at each state; thus, we assumed $\sigma_u/u = 10 \times 10^{-5}$.

4.1. Results for Helium

The helium was reported to be 99.9999 % pure. The Burnett apparatus was used to acquire $\rho(P, T)$ data on five quasi-isochores on six isotherms in the range 273.15 to 373.15 K. The Burnett expansions were conducted at 373.15 K from an initial pressure of 4.6 MPa. A total of 51 $\rho(P, T)$ points is tabulated in the Appendix (Table AVI). The resonator was used to acquire $u(P, T)$ data on six isotherms between 225 and 400 K. A total of 118 points with pressures up to 1.5 MPa is tabulated in the Appendix (Table AI).

At relatively low densities, helium is a unique fluid for thermophysical properties measurements. State-of-the-art *ab initio* calculations of the interaction energy between a pair of helium atoms are sufficiently accurate that

one can calculate the second virial coefficient and the transport properties with greater accuracy than can be achieved in measurements. We used the He-He two-body potential of Aziz *et al.* [22]. To calculate the second virial coefficient. Details of the calculation will be published elsewhere. The results were represented by the polynomial

$$B = 11.885370 + 6.6508722 \times 10^{-3} T - 3.205894 \times 10^{-5} T^2 \\ + 3.1354694 \times 10^{-8} T^3 \quad (10)$$

for the range $210 \leq T \leq 400$ K, where B is in $\text{cm}^3 \cdot \text{mol}^{-1}$ and T is in K. The third density virial coefficient was calculated by summing over only additive contributions to the three-body interactions. At the high reduced temperatures of our measurements, the nonadditive contributions to three-body interactions are small. This is consistent with the agreement between the calculated third density virial coefficient and previously published experimental values. The third virial coefficient was represented by the function

$$C = 44.2846 + 2.379099 \times 10^4 T^{-1} - 1.6689669 \times 10^6 T^{-1} \quad (11)$$

for the range $210 \leq T \leq 400$ K, where C is in $\text{cm}^6 \cdot \text{mol}^{-2}$ and T is in K.

We used the values of $B(T)$ and $C(T)$ calculated from the *ab initio* potential as a baseline for examining the experimental values of both the isochoric Burnett data and the speed-of-sound with other data. The deviations of the speed-of-sound data from the *ab initio* results are shown in Fig. 2. For the isotherms from 225 to 300 K, the speed-of-sound data agree

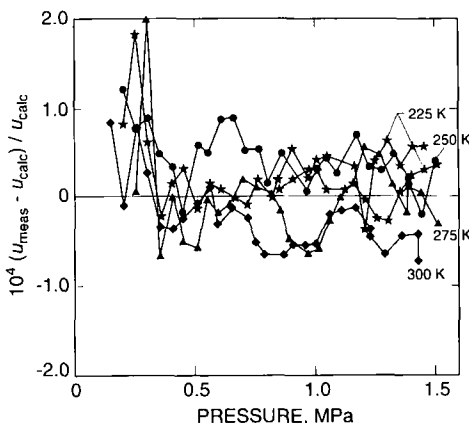


Fig. 2. Fractional deviations of speed-of-sound data from the *ab initio* calculations for helium. (◆) 300 K; (▲) 275 K; (●) 250 K; (★) 225 K.

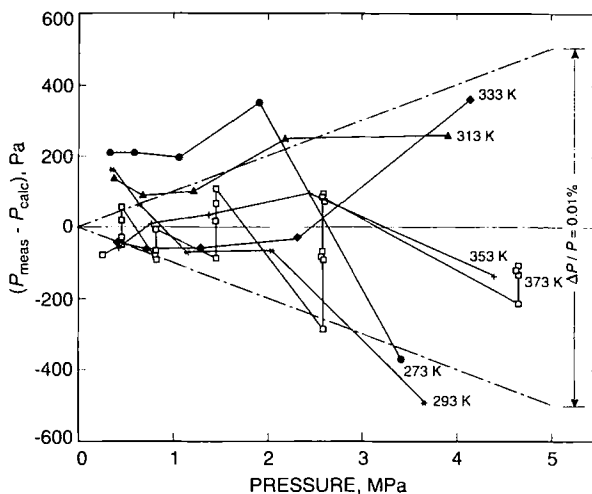


Fig. 3. Deviations of the $\rho(P, T)$ data from the ab initio calculations for helium. Most of the data are bounded by the dashed curves indicating $\pm 0.01\%$ of the pressure. (\square) 373.15 K; (+) 353.15 K; (\blacklozenge) 333.15 K; (\blacktriangle) 313.15 K; (*) 293.15 K; (\bullet) 273.15 K.

with the *ab initio* results to within $\pm 0.01\%$ of u . For the isotherms at 350 and 400 K (not shown) affected by a structural resonance, the agreement was within $\pm 0.035\%$. We emphasize that no parameters were fit to the data displayed in Fig. 2; the comparison with the *ab initio* results is on an absolute basis.

The isochoric-Burnett data are compared to *ab initio* results in Fig. 3. Nearly all the data fall within the dashed lines indicating $\pm 0.01\%$ of the pressure. The good agreement between the helium data and the *ab initio* results confirms the accuracy of our experimental techniques.

4.2. Results for Xenon

According to the manufacturer, the xenon sample had a purity of 99.9982%. It was degassed before use. In a preliminary analysis, we assumed that $\gamma^0 \equiv 5/3$ and we fit Eq. (6) each of the 11 isotherms, thereby determining the apparent molecular weight of the xenon m_{Xe} . The result was $m_{Xe} = (0.13126, \pm 0.00001_4) \text{ kg} \cdot \text{mol}^{-1}$, where the uncertainty cited is the standard deviation for all the isotherms. This result is marginally smaller than the value $0.13129 \text{ kg} \cdot \text{mol}^{-1}$ for xenon with the relative isotopic abundances found in air.

The speed of sound was measured in the xenon sample along 11 isotherms between 210 and 400 K, with the 400 K isotherm being repeated. The maximum pressure was limited to 1.5 MPa or 80% of the vapor pressure of xenon. The minimum pressure measured depended on the signal-to-noise ratio and typically was 0.05 MPa. In all, 288 speed-of-sound measurements were recorded as tabulated in the Appendix (Table AII).

The $\rho(P, T)$ measurements were made along four isotherms: 258.15, 303.15, 288.15, and 273.15 K. A total of 45 points with pressure up to 3.5 MPa was taken and tabulated in the Appendix (Table AVII).

The $\rho(P, T)$ data and the $u(P, T)$ data were simultaneously fit to a single density virial equation of state. The temperature dependencies of $B(T)$ and $C(T)$ were assumed to be those of the model hard-core square-well intermolecular potential. For $B(T)$, we used

$$\begin{aligned} B(T) &= b_0[1 - (\lambda^3 - 1)\Delta] \\ \Delta &= e^{\varepsilon/k_B T} - 1 \end{aligned} \quad (12)$$

and the best-fit parameters were $b_0 = 5.796870 \times 10^{-65} \text{ m}^3 \cdot \text{mol}^{-1}$, $\lambda = 1.693962$, and $\varepsilon/k_B = 181.76386 \text{ K}$. For $C(T)$, we used

$$\begin{aligned} C(T) &= \frac{1}{8}b_0^2(5 - c_1\Delta - c_2\Delta^2 - c_3\Delta^3) \\ c_1 &= \lambda^6 - 18\lambda^4 + 32\lambda^3 - 15 \\ c_2 &= 2\lambda^6 - 36\lambda^4 + 32\lambda^3 + 18\lambda^2 - 16 \\ c_3 &= 6\lambda^6 - 18\lambda^4 + 18\lambda^2 - 6 \\ \Delta &= e^{\varepsilon/k_B T} - 1 \end{aligned} \quad (13)$$

and the best-fit parameters were $b_0 = 7.573128 \times 10^{-65} \text{ m}^6 \cdot \text{mol}^{-1}$, $\lambda = 1.554699$, and $\varepsilon/k_B = 200.88133 \text{ K}$. The resulting fit had a $\chi^2 = 355$ with 329 degrees of freedom (df), yielding a $\chi^2/\text{df} = 1.08$. The $u(P, T)$ data had an RMS percentage deviation of 0.0020%, while the $\rho(P, T)$ data had an RMS percentage deviation of 0.011%.

Figure 4 shows the deviations of the speed-of-sound data from the fitted equation of state. Figure 5 shows the deviations of the $\rho(P, T)$ data from the fitted equation of state. The lines in Fig. 5 display 0.02% of the pressure. The deviations in Fig. 5 increase at pressure above 2 MPa and show a systematic temperature dependence. Most likely, these larger deviations result from the fourth density virial coefficient, $D(T)$. In fitting the xenon data, we neglected the data above 2 MPa and did not include a $D(T)$ term.

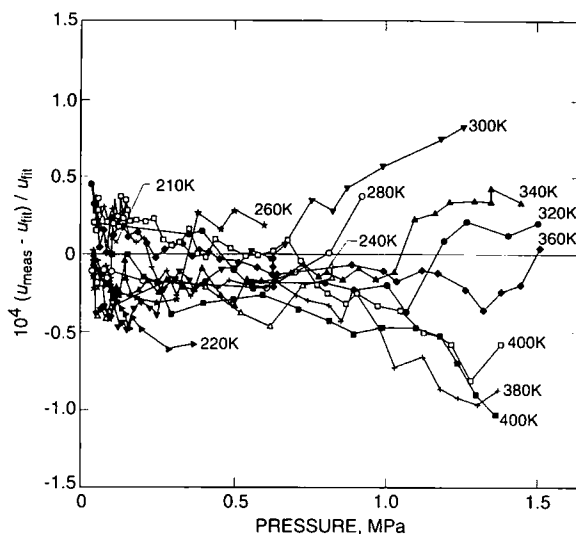


Fig. 4. Fractional deviations of the speed-of-sound data from the virial equation of state for xenon. (■, □) 400 K; (+) 380 K; (◆) 360 K; (▲) 340 K; (●) 320 K; (▼) 300 K; (○) 280 K; (★) 260 K; (►) 220 K; (×) 210 K.

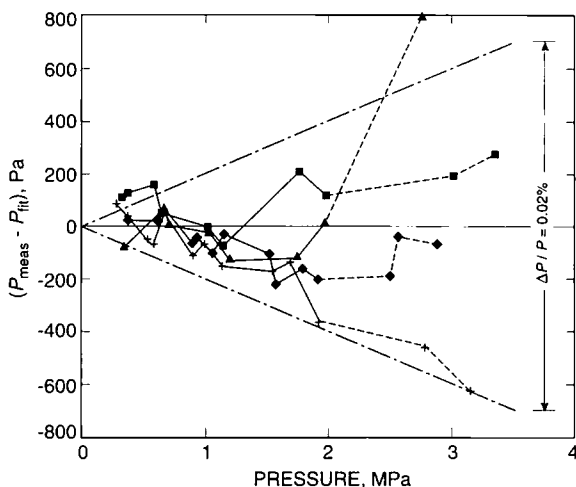


Fig. 5. Deviations of the $p(P, T)$ data from the virial equation of state for xenon. Most of the data are bound by the dashed curves indicating $\pm 0.02\%$ of the pressure. (■) 358.15 K; (+) 303.15 K; (◆) 288.15 K; (▲) 273.15 K.

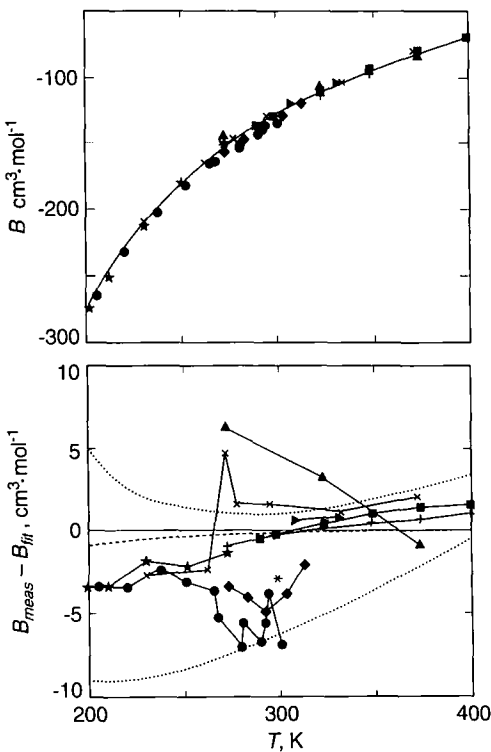


Fig. 6. Top: Second density virial coefficient $B(T)$ for xenon. Bottom: Deviations of $B(T)$ from Eq. (12) using the data reported in this work. (.....) Error bounds from Ref. 29; (----) calculated from HFD-B interatomic potential [23]. Published data: (■) Ref. 20; (+) Ref. 31; (◆) Ref. 32; (▲) Ref. 33; (*) Ref. 34; (●) Ref. 35; (★) Ref. 36; (►) Ref. 37; (×) Ref. 38.

Figure 6 compares $B(T)$ from Eq. (12) with published data and with the values of $B(T)$ calculated from a realistic intermolecular potential of Aziz *et al.* [23]. Below 270 K, the present values of $B(T)$ are less negative than previously published values and very close to the potential that was deduced from many properties. In contrast with previous low-temperature data, the present data permitted an analysis that included $C(T)$ and this may account for the differences.

Figure 7 compares $C(T)$ for xenon from the fit of Eq. (13) to the present data with previously published results and with a calculation based on the aforementioned potential. The calculated values for $C(T)$ did not

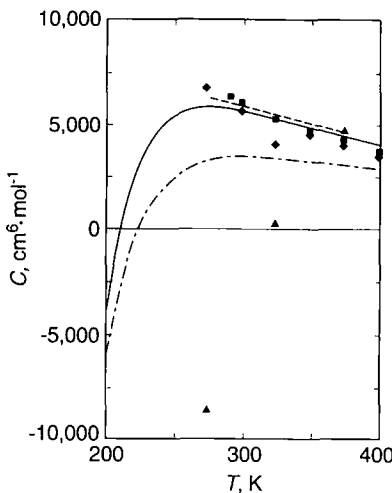


Fig. 7. Third density virial coefficient $C(T)$ for xenon. (—) This work, both $u(P, T)$ and $\rho(P, T)$ data; (----) this work, only $\rho(P, T)$ data with $D(T)$ included in the analysis; (-----) calculated from additive terms with HFD-B two-body potential [23]. Published data: (■) Ref. 30; (◆) Ref. 31; (▲) Ref. 33.

include the nonadditive component of the three-body interactions. Published calculations of the nonadditive effects [24] show that they are positive and of the correct magnitude to place the calculated $C(T)$ within a few percent of our current value. The dashed curve in Fig. 7 is based on the present $\rho(P, T)$ data only and was obtained from a fit to those data that included a single, temperature-independent parameter to represent $D(T)$. Thus the dashed curve shows the sensitivity of the derived quantity $C(T)$ to the neglect of $D(T)$ in our analysis that used both the $\rho(P, T)$ data and the $u(P, T)$ data.

4.3. Results for Helium–Xenon Mixtures

The three helium–xenon mixtures studied had been ordered from the manufacturer with the nominal compositions of 75/25, 50/50, and 25/75 mol% of helium to xenon. When attempting to fit these data for interaction virial coefficients, it became apparent that the nominal compositions were not accurate. This was confirmed by the speed-of-sound data. Therefore, we used Eq. (6) to extrapolate the speed-of-sound data to

zero pressure to determine the average molecular weight of each mixture. The resulting mole fractions of helium were $x_{\text{He}} = 0.74128$, 0.47304, and 0.20120.

The speed of sound was measured along nine isotherms between 225 and 400 K for each of the three helium–xenon mixtures. A total of 441 speed-of-sound measurements with pressures ranging between 0.4 to 1.5 MPa or 80% of the vapor pressure of xenon was considered (Tables AIII–AV). The Burnett $\rho(P, T)$ measurements were made along six isotherms between 273 and 373 K for each mixture. A total of 156 points was taken up to a pressure of 5 MPa (Tables AVIII–AX).

The $u(P, T)$ and $\rho(P, T)$ measurements for all three mixtures were simultaneously fit to a single equation of state to determine the helium–xenon interaction second and third density virial coefficients, $B_{12}(T)$, $C_{112}(T)$, and $C_{122}(T)$. The second and third density virial coefficients for the mixture as used in Eq. (1) are given by

$$\begin{aligned} B_{\text{mix}}(T)x_1^2B_{11}(T) + 2x_1x_2B_{12}(T) + x_2^2B_{22} \\ C_{\text{mix}}(T) = x_1^3C_{111}(T) + 3x_1^2x_2C_{112}(T) + 3x_1x_2^2C_{122}(T) + x_2^3C_{222}(T) \end{aligned} \quad (14)$$

Here x_1 and x_2 denote the mole fractions of helium and xenon, respectively, and the second density virial coefficients of helium and xenon are denoted $B_{11}(T)$ and $B_{22}(T)$. The second interaction density virial coefficient for helium–xenon interactions is $B_{12}(T)$. For the third density virial coefficient there are $C_{111}(T)$ and $C_{222}(T)$ for three-body He–He–He and Xe–Xe–Xe interactions and $C_{112}(T)$ and $C_{122}(T)$ for He–He–Xe and He–Xe–Xe interactions. The helium density virial coefficients $B_{11}(T)$ and $C_{111}(T)$ are known from the *ab initio* calculations, and the xenon $B_{22}(T)$ and $C_{222}(T)$ were determined from the xenon data and are given by Eqs. (10) and (11). Hence, $B_{12}(T)$, $C_{112}(T)$, and $C_{122}(T)$ were the only parameters adjusted to fit the mixture data.

Because the mixture data are at high reduced temperatures ($\varepsilon_{\text{He-Xe}}/k_B T \approx 30$), the hard-core square-well functions are not appropriate. For simplicity, we used polynomial functions of $(1/T)$ to represent the temperature dependencies of $B_{12}(T)$, $C_{112}(T)$, and $C_{122}(T)$; a cubic equation was used for $B_{12}(T)$ and linear equations were used for $C_{112}(T)$ and $C_{122}(T)$. Thus eight coefficients were adjusted to fit six sets of mixture data, that is, the $u(P, T)$ data and the $\rho(P, T)$ data for three compositions. The results are

$$B(T) \quad \text{or} \quad C(T) = \sum_{i=0}^n \frac{A_i}{T^i} \quad (15)$$

where B is in $\text{m}^3 \cdot \text{mol}^{-1}$, C is in $\text{m}^6 \cdot \text{mol}^{-2}$, and T is in K, with the following coefficients.

	$B_{12}(T)$	$C_{112}(T)$	$C_{122}(T)$
A_0	2.756941×10^{-5}	$-2.692605 \times 10^{-10}$	4.984636×10^{-10}
A_1	4.617880×10^{-3}	1.340259×10^{-7}	2.256122×10^{-7}
A_2	-1.741538	0.0	0.0
A_3	1.364453×10^2	0.0	0.0

The resulting fit had a $\chi^2 = 411$ with 370 df, yielding a $\chi^2/(\text{df}) = 1.11$. The speed-of-sound measurements had a RMS percentage deviation of 0.003 %,

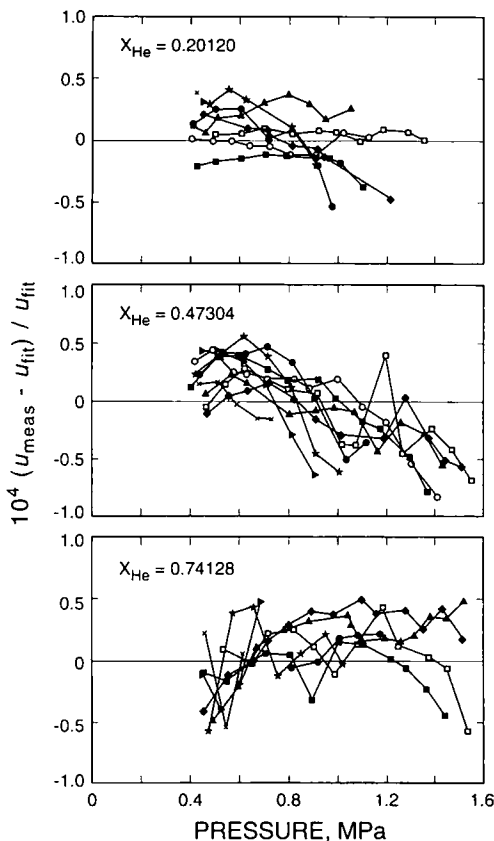


Fig. 8. Deviations of speed-of-sound data for helium-xenon mixtures from the present virial equation of state. (■) 400 K; (□) 375 K; (▲) 325 K; (○) 300 K; (●) 275 K; (★) 250 K; (►) 225 K; (×) 210 K.

while the Burnett $\rho(P, T)$ data fit the model with a RMS percentage deviation of 0.013 %. Figures 8 and 9 show the deviations of the speed-of-sound data and the Burnett $\rho(P, T)$ data from the fitted equation of state. Both figures shows that the virial equation of state fits the mixture data about as well as it fits the data for the pure components.

The published results for $B_{12}(T)$ in this temperature range that we are aware of are shown in Fig. 10, together with the results of caluclations from realistic intermolecular potential functions. The present values for $B_{12}(T)$ are within $1 \text{ cm}^3 \cdot \text{mol}^{-1}$ of those calculated from the two intermolecular potentials determined from elaborate multiproperty fits, namely, those of Aziz et al. [5] and Keil et al. [26]. The present values of $B_{12}(T)$ are as much as $3 \text{ cm}^3 \cdot \text{mol}^{-1}$ less negative than both a corresponding-states [7] model and a calculation by Hurly et al. [8] using an interatomic potential deduced from a multiproperty fit that put substantial weight on the thermal diffusion data that they acquired.

No published results were found for the third interaction density virial coefficients. The values of $C_{112}(T)$ and $C_{122}(T)$ resulting from the fit have the same order of magnitudes as the values calculated from the realistic intermolecular potential functions omitting three-body effects. The values

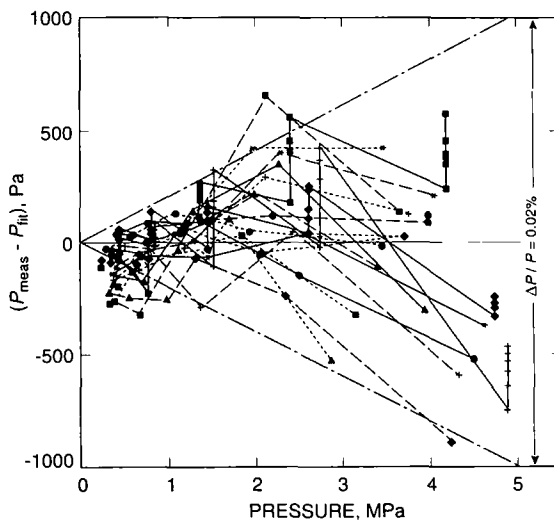


Fig. 9. Deviations of $\rho(P, T)$ data for helium-xenon mixtures from the virial equation of state. Most of the data are bounded by the dashed curves indicating $\pm 0.02\%$ of the pressure. (■) 373.15 K; (+) 353.15 K; (◆) 313.15 K; (▲) 293.15 K; (*) 300 K; (●) 273.15 K; (—) $x_{\text{He}} = 0.7413$; (---) $x_{\text{He}} = 0.4731$; (- - -) $x_{\text{He}} = 0.2014$.

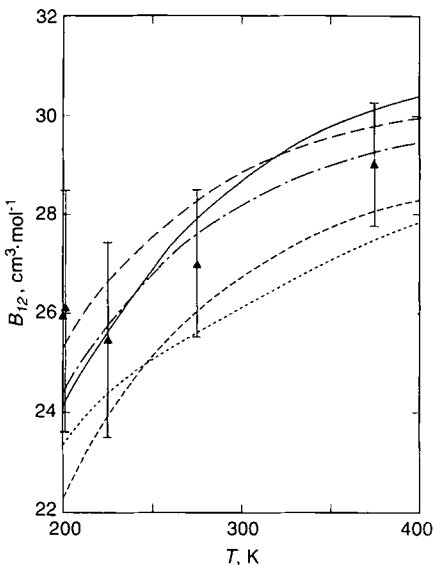


Fig. 10. Interaction second density virial coefficient $B_{12}(T)$ for helium-xenon mixtures. (—) Present fit to $u(P, T)$ data and $\rho(P, T)$ data; (\blacktriangle) Ref. 39. Calculated from interatomic potentials: (----) Ref. 40; (- - -) Ref. 41; (- - -) Ref. 42; (-----) law of corresponding states [27].

of $C_{112}(T)$ were not very well determined by the fit. When a term proportional to $1/T^2$ was included in the fit, the magnitude of $C_{112}(T)$ nearly doubled.

5. SUMMARY

Nearly all the present $u(P, T)$ and Burnett $\rho(P, T)$ data for helium agree with the *ab initio* calculated values to within $\pm 0.01\%$. The only parameter adjusted to achieve this agreement was the cell constant used in the Burnett data reduction. This is an unusual, independent demonstration of the accuracy of these experimental techniques.

The second virial coefficient presented for xenon agrees with previously published results and has a reduced uncertainty. The present results for the third virial coefficient of xenon extend the temperature range for this quantity by 60 down to 210 K. The data imply that $C(T)$ changes sign in this region. The equation of state for xenon using the presented $B(T)$ and $C(T)$ reproduces the speed-of-sound data to within $\pm 0.01\%$ and the Burnett $\rho(P, T)$ data to within $\pm 0.02\%$.

Prior to this work the best estimate of $B_{12}(T)$ for helium–xenon mixtures was obtained from the law of corresponding states. The present measurements on the three helium–xenon mixtures in conjunction with our accurate measurements on pure components have provided more direct information about this quantity as well as $C_{112}(T)$ and $C_{122}(T)$ from 210 to 400 K. The virial equation of state in three mixtures of differing composition reproduces nearly all the $u(P, T)$ data to within $\pm 0.01\%$ and nearly all of the Burnett $\rho(P, T)$ data to within $\pm 0.02\%$.

The density virial equation of state, Eq. (1), with the values of the virial coefficients given by Eqs. (10)–(15), provides an accurate representation of both the equation of state and the speed of sound in helium–xenon mixtures under the conditions of these experiments; thus, this equation of state is appropriate for the design of thermoacoustic refrigerators that operate under these conditions.

APPENDIX

Table AI. Helium Speed-of-Sound Results

P (kPa)	u (m · s ⁻¹)
$T = 400.00$ K	
1507.33	1182.215
1417.68	1181.894
1417.63	1181.882
1336.35	1181.597
1336.27	1181.609
1259.71	1181.327
1187.58	1181.093
1119.79	1180.889
1119.72	1180.855
1055.70	1180.618
995.41	1180.409
938.73	1180.227
885.37	1180.055
835.19	1179.873
787.95	1179.732
743.47	1179.550
701.56	1179.435
662.08	1179.289
594.45	1179.051
561.12	1178.947

Table AI. (*Continued*)

<i>P</i> (kPa)	<i>u</i> (m · s ⁻¹)
<i>T</i> = 350.00 K	
1516.59	1106.812
1435.80	1106.545
1358.67	1106.193
1286.00	1105.942
1285.95	1105.904
1217.30	1105.616
1091.10	1105.141
1033.10	1104.928
974.22	1104.732
974.18	1104.713
919.02	1104.515
867.17	1104.296
818.40	1104.150
734.90	1103.819
693.98	1103.650
655.56	1103.463
589.47	1103.238
557.17	1103.127
496.31	1102.885
442.84	1102.683
395.39	1102.563
353.92	1102.368
302.37	1102.156
248.66	1101.908
202.74	1101.872
<i>T</i> = 300.01 K	
1432.04	1025.584
1432.00	1025.614
1361.57	1025.299
1294.75	1024.983
1231.16	1024.720
1231.12	1024.725
1170.84	1024.484
1113.62	1024.226
1059.13	1023.979
1007.51	1023.717

Table A1. (*Continued*)

<i>P</i> (kPa)	<i>u</i> (m · s ⁻¹)
958.55	1023.496
912.22	1023.291
868.26	1023.084
791.68	1022.744
753.86	1022.589
718.08	1022.458
650.13	1022.167
594.26	1021.899
566.42	1021.817
448.68	1021.256
408.39	1021.065
357.32	1020.840
302.56	1020.657
256.90	1020.506
203.32	1020.178
152.69	1020.047
<i>T</i> = 275.00 K	
1509.23	982.985
1444.24	982.712
1381.71	982.424
1381.69	982.395
1321.77	982.144
1264.50	981.908
1210.05	981.658
1157.98	981.371
1108.24	981.121
1060.57	980.871
1015.12	980.626
971.66	980.417
895.25	980.070
875.25	979.922
820.90	979.766
757.55	979.477
699.36	979.209
646.11	978.931
597.27	978.691
552.42	978.493
509.14	978.235

Table A1. (*Continued*)

<i>P</i> (kPa)	<i>u</i> (m · s ⁻¹)
455.02	977.986
407.37	977.808
355.26	977.498
303.06	977.515
253.52	977.087
<i>T</i> = 250.00 K	
1504.83	938.097
1445.44	937.741
1388.03	937.486
1388.01	937.493
1332.80	937.238
1279.81	936.953
1229.02	936.701
1180.38	936.491
1094.08	936.015
1051.11	935.816
1009.78	935.594
970.13	935.369
865.13	934.881
803.69	934.539
772.55	934.418
714.97	934.125
665.00	933.909
616.29	933.661
554.36	933.313
514.97	933.121
451.28	932.729
408.93	932.564
351.68	932.288
304.35	932.087
252.34	931.812
203.49	931.607
<i>T</i> = 225.00 K	
1459.39	890.674
1406.10	890.386
1354.65	890.087
1305.22	889.847

Table AI. (*Continued*)

<i>P</i> (kPa)	<i>u</i> (m · s ⁻¹)
1257.76	889.570
1212.17	889.254
1168.12	889.081
1050.16	888.449
1012.21	888.241
975.69	888.026
910.98	887.704
841.04	887.349
820.76	887.167
767.16	886.894
717.37	886.600
668.20	886.340
605.10	886.007
564.78	885.793
512.78	885.488
453.97	885.208
403.73	884.921
359.47	884.647
305.12	884.428
255.44	884.265
204.63	883.900
<i>T</i> = 225.00 K	
1509.86	890.929
1455.66	890.631
1402.72	890.338
1351.65	890.045
1302.64	889.751
1255.48	889.500
1210.07	889.273
1166.52	889.052
1124.44	888.820
1049.53	888.414
1011.85	888.228
975.54	888.033
911.44	887.677
851.98	887.345

Table AII. Xenon Speed-of-Sound Results

<i>P</i> (kPa)	<i>u</i> (m · s ⁻¹)
<i>T</i> = 399.97 K	
1364.612	204.1431
1301.380	204.2021
1241.236	204.2601
1184.038	204.3155
1129.939	204.3651
1048.843	204.4425
976.032	204.5105
909.439	204.5743
868.833	204.6112
810.324	204.6676
774.019	204.7032
722.993	204.7549
676.685	204.8020
633.559	204.8421
582.680	204.8907
537.790	204.9342
492.404	204.9795
442.036	205.0301
411.214	205.0581
383.429	205.0859
355.895	205.1165
326.018	205.1444
297.737	205.1722
269.100	205.2015
240.908	205.2326
212.088	205.2610
183.074	205.2905
161.717	205.3118
153.052	205.3222
145.117	205.3316
138.123	205.3360
131.265	205.3459
124.873	205.3484
118.747	205.3556
112.931	205.3641
107.435	205.3664
87.161	205.3873
56.051	205.4187
56.033	205.4221
56.020	205.4201
51.526	205.4224
41.300	205.4339

Table AII. (*Continued*)

<i>P</i> (kPa)	<i>μ</i> (m · s ⁻¹)
<i>T</i> = 379.97 K	
1250.580	198.6398
1190.430	198.7158
1133.506	198.7911
989.286	198.9767
821.925	199.1928
753.884	199.2808
717.720	199.3280
613.234	199.4644
550.459	199.5465
494.239	199.6205
453.453	199.6729
407.571	199.7339
336.625	199.8275
288.810	199.8924
239.741	199.9580
189.620	200.0280
166.220	200.0599
130.708	200.1092
119.084	200.1243
108.484	200.1406
96.312	200.1554
82.565	200.1756
57.304	200.2108
<i>T</i> = 359.98 K	
1449.569	192.4631
1386.931	192.5666
1269.588	192.7629
1174.707	192.9241
1124.127	193.0096
1041.248	193.1480
996.103	193.2255
909.423	193.3733
640.289	193.8307
629.714	193.8500
629.320	193.8497
628.908	193.8524
628.557	193.8509
628.315	193.8522
628.306	193.8513

Table AII. (*Continued*)

<i>P</i> (kPa)	<i>u</i> (m · s ⁻¹)
578.364	193.9378
517.830	194.0424
455.486	194.1501
419.957	194.2122
387.641	194.2680
358.703	194.3173
332.185	194.3645
302.145	194.4163
271.342	194.4691
244.708	194.5142
212.436	194.5719
183.490	194.6235
153.682	194.6745
133.432	194.7111
120.730	194.7332
108.731	194.7528
96.346	194.7766
83.317	194.7949
71.918	194.8175
60.525	194.8353
57.371	194.8430
54.407	194.8482
51.577	194.8540
<i>T</i> = 339.98 K	
1359.32	186.439
1359.10	186.437
1303.14	186.561
1222.55	186.741
1176.11	186.844
1103.67	187.003
918.05	187.415
814.83	187.543
733.37	187.827
743.91	188.026
599.06	188.126
553.43	188.227
462.40	188.428
402.93	188.563
372.50	188.628
343.40	188.693

Table AII. (*Continued*)

<i>P</i> (kPa)	<i>u</i> (m · s ⁻¹)
313.15	188.760
283.64	188.826
254.21	188.890
224.31	188.958
194.43	189.023
164.94	189.088
151.24	189.120
136.95	189.152
130.93	189.164
125.24	189.176
119.78	189.189
114.69	189.200
109.86	189.210
105.24	189.220
100.89	189.230
<i>T</i> = 319.99 K	
990.36	181.004
874.70	181.334
762.55	181.655
720.94	181.773
667.99	181.923
618.61	182.062
559.85	182.229
507.73	182.376
461.62	182.505
408.72	182.653
318.66	182.908
270.59	183.043
243.43	183.118
219.20	183.187
191.03	183.266
167.42	183.332
133.30	183.427
107.50	183.501
95.41	183.534
83.41	183.569
69.72	183.608
58.06	183.640
45.38	183.676

Table AII. (*Continued*)

<i>P</i> (kPa)	<i>u</i> (m · s ⁻¹)
<i>T</i> = 299.99 K	
1205.75	173.589
1078.86	174.065
1014.03	174.309
905.59	174.712
808.53	175.071
571.29	175.936
507.72	176.164
402.09	176.547
357.63	176.705
208.78	177.235
81.22	177.683
58.63	177.765
58.63	177.765
715.55	168.681
506.49	169.658
413.46	170.086
309.32	170.561
204.14	171.035
80.03	171.588
66.42	171.648
53.03	171.708
<i>T</i> = 260.00 K	
919.07	160.214
824.90	160.815
720.67	161.468
605.14	162.176
507.81	162.762
313.23	163.906
245.84	164.294
175.69	164.695
103.42	165.103
92.92	165.163
82.21	165.224
71.84	165.281
61.01	165.341
51.22	165.397
41.28	165.453
41.12	165.454
41.12	165.455

Table AII. (*Continued*)

<i>P</i> (kPa)	<i>u</i> (m · s ⁻¹)
41.12	165.453
41.12	165.453
41.28	165.453
41.12	165.453
<i>T</i> = 240.01 K	
1030.42	150.935
913.86	151.992
826.52	152.762
826.42	152.672
729.43	153.593
523.93	155.277
360.44	156.546
226.05	157.556
164.16	158.006
100.86	158.466
90.55	158.539
76.91	158.636
65.36	158.719
52.95	158.806
<i>T</i> = 220.01 K	
454.93	147.976
293.43	149.630
206.21	150.485
151.41	151.009
136.72	151.148
117.02	151.333
100.11	151.492
56.80	151.895
<i>T</i> = 209.97 K	
197.82	146.777
133.44	147.478
94.36	147.896
81.13	148.036
66.59	148.190
54.71	148.314
41.05	148.457
41.04	148.458
41.04	148.458
41.03	148.457
40.90	148.460

Table AIII. He/Xe ($x_{\text{He}} = 0.74128$)
Speed-of-Sound Results

<i>P</i> (kPa)	<i>u</i> (m · s ⁻¹)
<i>T</i> = 399.97 K	
1527.25	390.326
1442.77	290.175
1362.11	390.030
1286.25	389.892
1166.47	389.668
1101.33	389.546
995.41	389.344
899.63	389.143
814.37	388.994
710.60	388.796
639.84	388.658
551.89	388.484
456.35	388.303
373.20	388.139
292.75	387.964
202.56	387.747
153.37	387.624
139.59	387.617
119.40	387.598
<i>T</i> = 374.97 K	
1532.88	378.051
1452.31	377.914
1375.21	377.768
1253.30	377.536
1186.75	377.419
1081.61	377.204
986.58	377.010
900.20	376.852
817.90	376.698
718.29	376.503
628.47	376.321
540.26	376.154

Table AIII. (*Continued*)

<i>P</i> (kPa)	<i>u</i> (m · s ⁻¹)
<i>T</i> = 349.98 K	
1512.01	365.313
1429.32	365.160
1350.85	365.000
1276.67	364.860
1161.87	364.634
1097.99	364.513
984.32	364.286
894.65	364.111
801.71	363.925
718.84	363.759
645.13	363.608
553.50	363.425
457.90	363.228
375.56	363.038
200.71	362.621
179.26	362.573
170.00	362.557
152.03	362.524
136.28	362.495
122.38	362.471
110.07	362.454
94.38	362.429
81.25	362.411
<i>T</i> = 299.98 K	
1449.12	338.347
1381.67	338.212
1317.19	338.078
1255.60	337.954
1196.70	337.837
1102.95	337.650
1051.78	337.552
1044.70	337.541
882.08	337.172

Table AIII. (*Continued*)

<i>P</i> (kPa)	<i>u</i> (m · s ⁻¹)
783.17	336.974
669.44	336.745
591.64	336.582
493.25	336.380
397.57	336.167
301.15	335.953
203.69	335.708
181.07	335.642
172.95	335.623
160.11	335.590
148.18	335.560
137.10	335.531
126.19	335.505
115.71	335.481
103.82	335.450
93.71	335.422
82.23	335.388
<i>T</i> = 274.00 K	
1175.79	323.477
1086.99	323.301
1005.80	323.139
919.95	322.964
815.35	322.758
381.95	321.847
292.03	321.654
202.66	321.400
185.20	321.360
163.88	321.298
145.27	321.239
127.52	321.187
107.70	321.125
<i>T</i> = 250.01 K	
1026.57	308.211
955.44	308.081

Table AIII. (*Continued*)

<i>P</i> (kPa)	<i>u</i> (m · s ⁻¹)
854.71	307.882
763.82	307.703
660.31	307.523
572.29	307.355
478.47	307.150
386.49	306.955
292.46	306.752
200.92	306.543
180.23	306.483
166.30	306.423
153.27	306.380
137.70	306.331
124.00	306.286
<i>T</i> = 225.01 K	
603.94	291.603
525.16	291.457
452.48	291.338
367.92	291.190
288.21	290.999
205.13	290.810
182.24	290.746
167.50	290.698
153.74	290.644
137.06	290.582
126.04	290.531
111.07	290.457
<i>T</i> = 210.01 K	
615.65	281.743
541.74	281.605
463.70	281.499
377.07	281.348
290.63	281.167
202.37	280.993
183.79	280.936
155.61	280.864
129.75	280.796
104.77	280.721
78.04	280.620

Table AIV. He/Xe ($x_{\text{He}} = 0.47304$)
Speed-of-Sound Results

P (kPa)	u ($\text{m} \cdot \text{s}^{-1}$)
$T = 399.97 \text{ K}$	
1294.74	280.697
1174.55	280.565
1107.87	280.491
992.76	280.365
924.50	280.291
799.05	280.149
716.50	280.058
597.86	279.928
498.02	279.816
401.29	279.701
309.04	279.592
205.61	279.460
153.04	279.393
134.02	279.379
117.47	279.378
99.81	279.351
82.43	279.337
68.73	279.327
51.14	279.313
$T = 374.97 \text{ K}$	
1553.79	271.981
1471.44	271.899
1391.19	271.817
1267.63	271.679
1198.68	271.628
1080.16	271.482
1021.62	271.421
919.93	271.327
799.02	271.203
719.28	271.122
624.72	271.028
541.31	270.939
467.48	270.859
369.73	270.752
292.55	270.666

Table AIV. (*Continued*)

<i>P</i> (kPa)	<i>u</i> (m · s ⁻¹)
205.53	270.565
148.95	270.490
133.45	270.476
119.85	270.468
103.56	270.450
89.16	270.437
73.39	270.421
56.99	270.403
<i>T</i> = 349.98 K	
1442.29	262.509
1375.73	262.450
1277.68	262.366
1188.82	262.273
1013.14	262.110
917.16	262.026
823.37	261.945
724.58	261.859
636.78	261.779
556.77	261.707
470.31	261.627
377.21	261.541
292.40	261.461
201.34	261.369
153.77	261.315
138.65	261.301
120.84	261.283
108.86	261.274
93.79	261.256
79.05	261.236
66.20	261.225
49.76	261.206
<i>T</i> = 324.99 K	
1434.00	252.747
1366.29	252.699
1260.37	252.618
1163.43	252.536

Table AIV. (*Continued*)

<i>P</i> (kPa)	<i>u</i> (m · s ⁻¹)
1073.05	252.476
989.91	252.414
913.24	252.356
809.23	252.279
633.52	252.159
557.75	252.107
460.84	252.036
377.37	251.976
287.74	251.908
204.09	251.834
154.34	251.776
136.76	251.766
121.43	251.751
107.96	251.741
92.25	251.726
77.52	251.709
64.92	251.697
<i>T</i> = 299.99 K	
1410.16	242.506
1301.49	242.450
1198.14	242.402
1104.62	242.355
997.62	242.304
880.21	242.243
820.90	242.215
718.74	242.166
629.39	242.125
569.11	242.097
497.47	242.070
420.28	242.033
342.77	241.994
275.94	241.956
204.77	241.908
152.48	241.867
136.24	241.853
117.75	241.835

Table AIV. (*Continued*)

<i>P</i> (kPa)	<i>u</i> (m · s ⁻¹)
105.43	241.824
88.16	241.809
70.28	241.789
<i>T</i> = 275.00 K	
1118.39	231.676
1036.25	231.656
908.59	231.646
817.56	231.638
714.14	231.627
623.98	231.614
529.51	231.604
432.12	231.591
340.31	231.575
242.33	231.557
153.72	231.526
141.96	231.523
123.56	231.512
107.59	231.503
91.89	231.492
77.37	231.471
65.99	231.464
<i>T</i> = 250.00 K	
1007.27	220.363
917.70	220.395
811.83	220.445
816.86	220.485
615.95	220.527
513.00	220.565
427.14	220.597
336.37	220.632
246.19	220.665
153.00	220.680
121.82	220.678
104.90	220.674
88.01	220.670

Table AIV. (*Continued*)

<i>P</i> (kPa)	<i>u</i> (m · s ⁻¹)
73.25	220.659
56.94	220.641
<i>T</i> = 225.01 K	
910.81	208.357
814.51	208.474
716.05	208.597
615.83	208.718
507.72	208.849
447.82	208.920
387.52	208.992
327.17	209.059
267.15	209.125
205.40	209.189
152.45	209.234
133.97	209.246
111.75	209.264
90.65	209.275
70.81	209.276
<i>T</i> = 210.01 K	
736.03	200.981
677.73	201.091
594.76	201.250
510.28	201.413
437.69	201.550
357.92	201.690
283.33	201.820
203.51	201.955
182.66	201.986
163.97	202.010
141.35	202.040
121.64	202.065
103.03	202.092
81.93	202.112
60.97	202.115

Table AV. He/Xe ($x_{\text{He}} = 0.20120$)
Speed-of-Sound Results

<i>P</i> (kPa)	<i>u</i> (m · s ⁻¹)
<i>T</i> = 399.97 K	
1103.49	229.049
1005.22	229.046
956.94	229.044
910.60	229.041
781.55	229.034
704.63	229.031
587.62	229.026
501.97	229.024
424.44	229.022
342.88	229.020
273.92	229.022
161.13	229.032
139.69	229.032
121.33	229.034
100.28	229.035
82.70	229.039
61.15	229.041
<i>T</i> = 374.98 K	
1356.56	221.454
1289.93	221.465
1186.08	221.482
1088.78	221.497
999.87	221.515
924.36	221.531
811.78	221.554
714.45	221.576
608.66	221.600
500.28	221.626
<i>T</i> = 349.98 K	
1216.79	213.535
943.84	213.685
942.86	213.685
920.80	213.699
817.13	213.756

Table AV. (*Continued*)

<i>P</i> (kPa)	<i>u</i> (m · s ⁻¹)
722.98	213.811
720.23	213.813
632.56	213.864
450.56	213.974
346.99	214.031
250.69	214.088
153.49	214.138
130.27	214.148
114.04	214.157
95.67	214.167
76.87	214.176
58.34	214.187
<i>T</i> = 324.99 K	
952.03	205.464
882.84	205.536
798.15	205.622
700.16	205.720
603.90	205.817
510.59	205.913
461.75	205.961
408.66	206.019
355.46	206.075
305.38	206.126
256.52	206.176
201.83	206.230
151.35	206.280
131.95	206.300
117.17	206.316
106.86	206.327
93.61	206.339
79.35	206.354
66.15	206.368
<i>T</i> = 299.99 K	
1126.17	196.489
1024.93	196.650
911.62	196.828

Table AV. (*Continued*)

<i>P</i> (kPa)	<i>u</i> (m · s ⁻¹)
809.47	196.993
720.61	197.138
640.59	197.269
559.45	197.402
485.73	197.423
405.83	197.654
358.45	197.731
308.58	197.811
251.27	197.907
205.32	197.982
151.36	198.068
140.72	198.086
115.36	198.125
91.63	198.164
65.44	198.205
<i>T</i> = 275.00 K	
917.93	187.632
810.49	187.903
714.03	188.138
608.95	188.404
499.85	188.673
410.65	188.891
350.86	189.038
299.70	189.165
254.77	189.273
202.28	189.400
154.03	189.513
137.51	189.550
117.48	189.598
92.12	189.656
66.97	189.716
<i>T</i> = 250.00 K	
915.51	177.708
814.70	178.093
625.91	178.802

Table AV. (*Continued*)

<i>P</i> (kPa)	<i>u</i> (m · s ⁻¹)
557.44	179.056
479.89	179.338
357.70	179.781
307.64	179.963
251.20	180.164
152.30	180.511
132.29	180.580
109.50	180.660
<i>T</i> = 225.01 K	
385.37	169.751
308.78	170.161
231.14	170.571
154.56	170.961
143.80	171.015
130.40	171.081
115.32	171.156
101.94	171.221
89.33	171.283
75.70	171.346
60.33	171.419
<i>T</i> = 210.01 K	
425.95	163.099
383.52	163.386
293.24	164.003
247.05	164.317
198.66	164.635
153.10	164.933
115.11	165.175
98.63	165.278
84.89	165.363
69.69	165.457
55.48	165.542

Table AVI. $P\rho T$ Burnett Results for
Helium

P (kPa)	ρ (mol · L ⁻¹)
$T = 373.15$ K	
4640.95	1.4706
4640.94	1.4706
4640.93	1.4706
4640.85	1.4706
2586.06	0.8256
2586.03	0.8256
2585.90	0.8256
2585.87	0.8256
2585.68	0.8256
1445.75	0.4635
1445.71	0.4635
1445.66	0.4635
1445.56	0.4635
1445.56	0.4635
809.64	0.2602
809.64	0.2602
809.58	0.2602
809.55	0.2602
809.55	0.2602
453.98	0.1461
453.94	0.1461
453.93	0.1461
453.89	0.1461
453.88	0.1461
254.57	0.0820
$T = 353.15$ K	
5396.34	1.4718
2449.63	0.8263
1369.34	0.4638
766.89	0.2604
429.90	0.1462
$T = 333.15$ K	
4151.73	1.4730
2312.81	0.8269
1292.79	0.4642
723.99	0.2606
405.90	0.1463

Table AVI. (*Continued*)

<i>P</i> (kPa)	<i>p</i> (mol · L ⁻¹)
<i>T</i> = 313.15 K	
3906.01	1.4742
2176.09	0.8276
1216.36	0.4646
681.22	0.2608
681.22	0.2608
382.01	0.1464
<i>T</i> = 293.15 K	
3659.14	1.4753
2038.53	0.8282
2038.53	0.8282
1139.42	0.4649
638.19	0.2610
357.91	0.1465
<i>T</i> = 273.15 K	
3412.63	1.4764
1901.44	0.8288
1062.79	0.4653
595.27	0.2612
333.81	0.1466

Table AVII. *PpT* Burnett Results for Xenon

<i>P</i> (kPa)	<i>p</i> (mol · L ⁻¹)
<i>T</i> = 358.15 K	
3352.55	1.2592
1975.57	0.7067
1139.64	0.3966
649.50	0.2225
367.61	0.1248
3013.69	1.1180
1766.41	0.6274
1015.86	0.3521
577.93	0.1975
326.78	0.1108

Table AVII. (*Continued*)

P (kPa)	ρ (mol · L ⁻¹)
$T = 303.15\text{ K}$	
3147.73	1.5204
1927.96	0.8532
1135.28	0.4787
654.21	0.2685
372.48	0.1506
2796.94	1.3147
1692.27	0.7377
989.83	0.4139
568.27	0.2322
1546.60	0.6682
900.29	0.3749
516.12	0.2103
292.87	0.1179
$T = 288.15\text{ K}$	
1922.38	0.9140
1142.98	0.5128
661.93	0.2876
377.88	0.1613
2502.26	1.2501
1521.52	0.7014
892.05	0.3935
2572.76	1.2936
1569.00	0.7259
921.34	0.4072
2879.87	1.4917
1780.32	0.8370
1053.09	0.4696
608.26	0.2634
$T = 273.15\text{ K}$	
2757.93	1.5699
1738.89	0.8809
1038.75	0.4942
603.06	0.2772
344.70	0.1555
1961.15	1.0159
1183.53	0.5700
690.86	0.3197

Table AVIII. $P\rho T$ Burnett Results for
He/Xe ($x_{\text{He}} = 0.20120$)

P (kPa)	ρ (mol · L ⁻¹)
$T = 373.15 \text{ K}$	
4213.32	1.4377
4213.32	1.4377
4213.20	1.4377
4213.14	1.4377
4213.13	1.4377
4213.10	1.4377
4212.98	1.4377
2423.10	0.8071
2423.00	0.8071
2422.95	0.8071
2422.72	0.8071
1379.68	0.4531
1379.67	0.4531
1379.65	0.4531
1379.62	0.4531
1379.54	0.4531
1379.51	0.4531
780.80	0.2544
780.69	0.2544
780.63	0.2544
780.52	0.2544
440.31	0.1428
440.29	0.1428
440.26	0.1428
440.23	0.1428
440.15	0.1428
247.75	0.0802
$T = 353.15 \text{ K}$	
3951.25	1.4389
2282.50	0.8077
1302.73	0.4535
738.08	0.2546
416.52	0.1429
$T = 333.15 \text{ K}$	
3688.59	1.4400
2141.74	0.8084
1225.57	0.4538
695.31	0.2548
398.71	0.1430

Table AVIII. (*Continued*)

<i>P</i> (kPa)	<i>ρ</i> (mol · L ⁻¹)
<i>T</i> = 313.15 K	
3422.99	1.4411
1999.42	0.8090
1148.07	0.4542
652.80	0.2550
369.01	0.1431
<i>T</i> = 293.15 K	
3154.60	1.4422
1856.40	0.8096
609.84	0.2552
345.08	0.1432
<i>T</i> = 273.15 K	
2882.51	1.4433
1712.48	0.8102
991.90	0.4549
566.68	0.2553
321.22	0.1433

Table AIX. *PρT* Burnett Results for
He/Xe (*x*_{He} = 0.47304)

<i>P</i> (kPa)	<i>ρ</i> (mol · L ⁻¹)
<i>T</i> = 373.15 K	
4907.02	1.5907
4906.99	1.5907
4906.96	1.5907
4906.91	1.5907
4906.84	1.5907
4906.74	1.5907
2760.23	0.8930
2760.18	0.8930
2760.09	0.8930
2759.83	0.8930
2759.79	0.8930

Table AIX. (*Continued*)

<i>P</i> (kPa)	<i>p</i> (mol · L ⁻¹)
1551.90	0.5013
1551.77	0.5013
1551.75	0.5013
1551.72	0.5013
1551.48	0.5013
871.97	0.2814
871.95	0.2814
871.91	0.2814
871.90	0.2814
871.87	0.2814
489.75	0.1580
489.73	0.1580
489.73	0.1580
489.70	0.1580
489.69	0.1580
274.96	0.0887
<i>T</i> = 535.15 K	
4626.61	1.5920
2607.26	0.8937
1467.40	0.5017
825.08	0.2817
463.62	0.1581
<i>T</i> = 333.15 K	
4344.54	1.5933
254.12	0.8944
1382.81	0.5021
778.25	0.2819
437.50	0.1582
<i>T</i> = 313.15 K	
4061.99	1.5945
2300.75	0.8951
1298.47	0.5025
731.20	0.2821
411.19	0.1584
<i>T</i> = 293.15 K	
3776.72	1.5957
2146.23	0.8958

Table AIX. (*Continued*)

<i>P</i> (kPa)	<i>p</i> (mol · L ⁻¹)
1213.53	0.5029
684.08	0.2823
384.88	0.1585
<i>T</i> = 273.15 K	
3489.66	1.5969
1991.17	0.8965
1128.40	0.5033
636.89	0.2825
358.57	0.1586

Table AX. *PρT* Burnett Results for
He/Xe ($x_{\text{He}} = 0.74128$)

<i>P</i> (kPa)	<i>p</i> (mol · L ⁻¹)
<i>T</i> = 373.15 K	
4758.74	1.5048
4758.70	1.5048
2649.13	0.8448
2649.12	0.8448
2649.03	0.8448
2648.99	0.8448
2648.91	0.8448
1480.22	0.4742
1480.21	0.4742
1480.21	0.4742
1480.17	0.4742
1480.04	0.4742
828.86	0.2662
828.77	0.2662
828.75	0.2662
828.75	0.2662
828.71	0.2662
464.59	0.1495
464.56	0.1495

Table AX. (*Continued*)

<i>P</i> (kPa)	<i>p</i> (mol · L ⁻¹)
464.55	0.1495
464.53	0.1495
464.46	0.1495
260.49	0.0839
<i>T</i> = 353.15 K	
4502.32	1.5060
2507.29	0.8455
1401.48	0.4746
784.85	0.2664
440.00	0.1496
<i>T</i> = 333.15 K	
4245.05	1.5072
2365.38	0.8461
1322.47	0.4750
740.70	0.2667
415.19	0.1497
<i>T</i> = 313.15 K	
3988.39	1.5084
3988.35	1.5084
2223.57	0.8468
1243.60	0.4754
696.59	0.2669
390.57	0.1498
<i>T</i> = 293.15 K	
3729.83	1.5096
2080.89	0.8474
1164.38	0.4757
652.35	0.2671
365.82	0.1499
<i>T</i> = 273.15 K	
3470.49	1.5107
1938.08	0.8481
1085.06	0.4761
608.18	0.2673
341.09	0.1500

ACKNOWLEDGMENTS

The authors greatly appreciate the continuing interest and assistance provided by Keith Gillis on many phases of this work and Lloyd Weber for his critical reading of the manuscript. This research was supported in part by the Office of Naval Research.

REFERENCES

1. M. Waxman and J. R. Hastings, *J. Res. Natl. Bur. Stand.* **75C**:165 (1971).
2. D. Linsky, J. M. H. Levelt Sengers, and H. A. Davis, *Rev. Sci. Instrum.* **58**:817 (1987).
3. D. Linsky, J. M. H. Levelt Sengers, and J. S. Gallagher, *Fluid Phase Equil.* **36**:149 (1987).
4. M. Waxman and W. T. Chen, *J. Res. Natl. Bur. Stand.* **69C**:27 (1965).
5. D. E. Gray (Ed.), *The American Institute of Physics Handbook*, 3rd ed. (McGraw-Hill, New York, 1972), pp. 4-126.
6. M. R. Moldover, M. Waxman, and M. Greenspan, *High Temp. High Press.* **11**:75 (1979).
7. J. B. Mehl and M. R. Moldover, *J. Chem. Phys.* **74**:4062 (1981).
8. J. B. Mehl and M. R. Moldover, in *Proc. Eight Symp. Thermophys. Prop.*, J. V. Sengers, ed. (ASME, New York, 1982), pp. 134-141.
9. M. R. Moldover, J. B. Mehl, and M. Greenspan, *J. Acoust. Soc. Am.* **79**:253 (1986).
10. M. R. Moldover, J. P. M. Trusler, T. J. Edwards, J. B. Mehl, and R. S. Davis, *J. Res. Natl. Bur. Stand.* **93**:85 (1988).
11. J. P. M. Trusler, *Physical Acoustic and Metrology of Fluids* (Adam Hilger, Bristol, 1991).
12. A. R. H. Goodwin and M. R. Moldover, *J. Chem. Phys.* **93**:2741 (1990).
13. A. R. H. Goodwin and M. R. Moldover, *J. Chem. Phys.* **95**:5230 (1991).
14. A. R. H. Goodwin and M. R. Moldover, *J. Chem. Phys.* **95**:5236 (1991).
15. K. A. Gillis and M. R. Moldover, in *Proceedings of the Ninth Symposium on Energy Engineering Sciences*, Argonne National Laboratory, May 13-15 (U.S. Department of Energy Report CONF-9105116, National Technical Information Service, Springfield, VA, 1991), p. 310.
16. D. Desibaugh, K. A. Gillis, M. R. Moldover, G. Morrison, and J. W. Schmidt, *Fluid Phase Equil.* **81**:285 (1992).
17. K. A. Gillis, *Int. J. Thermophys.* **15**:821 (1994).
18. K. A. Gillis, A. R. H. Goodwin, and M. R. Moldover, *Rev. Sci. Instrum.* **62**:2213 (1991).
19. K. A. Gillis, in press.
20. K. A. Gillis and M. R. Moldover, *Int. J. Thermophys.* **17**:1305 (1996).
21. Private communication with K. A. Gillis.
22. R. A. Aziz, A. R. Janzen, and M. R. Moldover, *Phys. Rev. Lett.* **74**:1586 (1995).
23. K. Dharm, W. Meath, A. R. Allnatt, R. A. Aziz, and M. Slaman, *Chem. Phys.* **142**:173 (1990).
24. R. Pospisil, A. Malijevsky, and S. Labik, *Mol. Phys.* **64**:21 (1988).
25. R. A. Aziz, U. Buck, H. Jonsson, J. C. Ruiz-Suarez, B. Schmidt, G. Scoles, M. J. Slaman, and J. Xu, *J. Chem. Phys.* **91**:6477 (1989). [Errata: *J. Chem. Phys.* **93**:4493 (1990).]
26. M. Keil, L. Danielson, and P. J. Dunlop, *J. Chem. Phys.* **94**:296 (1991).
27. B. Najić, E. A. Mason, and J. Kestin, *Physica* **119A**:387 (1983).
28. J. J. Hurly, W. L. Taylor, and D. A. Menke, *J. Chem. Phys.* **94**:8282 (1991).
29. J. H. Dymond and E. B. Smith, *The Virial Coefficients of Pure Gases and Mixtures* (Clarendon Press, Oxford, 1980), pp. 251-254.
30. J. A. Beattie, R. J. Barriault, and J. S. Brierly, *J. Chem. Phys.* **19**:1222 (1951).

31. A. Michels, T. Wassenaar, and P. Louwerse, *Physica* **20**:99 (1954).
32. C. G. Reeves and R. Whytlaw-Gray, *Proc. Roy. Soc. A* **232**:173 (1955).
33. E. Whalley, Y. Lupien, and W. G. Schneider, *Can. J. Chem.* **33**:633 (1955).
34. C. M. Greenlief and G. Constabaris, *J. Chem. Phys.* **44**:4649 (1966).
35. C. A. Pollard and G. Saville, unpublished results, from C. A. Pollard, Ph.D. thesis (University of London, London, 1971).
36. R. Hahn, K. Shäfer, and B. Schramm, *Ber. Bunsenges. Phys. Chem.* **78**:287 (1974).
37. P. Rentschler and B. Schramm, *Ber. Bunsenges. Phys. Chem.* **81**:319 (1977).
38. B. Schramm, H. Schmiedel, R. Gehrmann, and R. Barth, *Ber. Bunsenges. Phys. Chem.* **81**:316 (1977).
39. J. Brewer, Air Force Office of Scientific Research, Report No. 67-2795 (1967).
40. J. J. Hurly, W. L. Taylor, and D. A. Menke, *J. Chem. Phys.* **94**:8282 (1991).
41. R. A. Aziz, U. Buck, H. Jonsson, J. C. Ruiz-Suarez, B. Schmidt, G. Scoles, M. J. Slaman, and J. Xu, *J. Chem. Phys.* **91**:6477 (1989). [Errata: *J. Chem. Phys.* **93**:4493 (1990).]
42. M. Keil, L. Danielson, and P. J. Dunlop, *J. Chem. Phys.* **94**:296 (1991).